







Single-cell analysis of patient-derived PDAC organoids reveals cell state heterogeneity and a conserved developmental hierarchy

Teresa G. Krieger^{1,2,7}, Solange Le Blanc^{3,4,5,7}, Julia Jabs^{2,7}, Foo Wei Ten ^{1,2}, Naveed Ishaque ¹, Katharina Jechow ^{1,2}, Olivia Debnath¹, Carl-Stephan Leonhardt³, Anamika Giri², Roland Eils ^{1,2,8}✉, Oliver Strobel ^{3,5,6,8}✉ & Christian Conrad ^{1,2,8}✉

Pancreatic ductal adenocarcinoma (PDAC) is projected to be the second leading cause of cancer mortality by 2030. Bulk transcriptomic analyses have distinguished ‘classical’ from ‘basal-like’ tumors with more aggressive clinical behavior. We derive PDAC organoids from 18 primary tumors and two matched liver metastases, and show that ‘classical’ and ‘basal-like’ cells coexist in individual organoids. By single-cell transcriptome analysis of PDAC organoids and primary PDAC, we identify distinct tumor cell states shared across patients, including a cycling progenitor cell state and a differentiated secretory state. Cell states are connected by a differentiation hierarchy, with ‘classical’ cells concentrated at the endpoint. In an imaging-based drug screen, expression of ‘classical’ subtype genes correlates with better drug response. Our results thus uncover a functional hierarchy of PDAC cell states linked to transcriptional tumor subtypes, and support the use of PDAC organoids as a clinically relevant model for in vitro studies of tumor heterogeneity.

¹Digital Health Center, Berlin Institute of Health (BIH)/Charité-Universitätsmedizin Berlin, Berlin, Germany. ²Division of Theoretical Bioinformatics, German Cancer Research Center (DKFZ), Heidelberg, Germany. ³European Pancreas Center, Department of General Surgery, Heidelberg University Hospital, Heidelberg, Germany. ⁴Division of Molecular Oncology of Gastrointestinal Tumors, German Cancer Research Center (DKFZ), Heidelberg, Germany. ⁵National Center for Tumor diseases (NCT), Heidelberg, Germany. ⁶Division of Visceral Surgery, Department of General Surgery, Medical University of Vienna, Vienna, Austria. ⁷These authors contributed equally: Teresa G. Krieger, Solange Le Blanc, Julia Jabs. ⁸These authors jointly supervised this work: Roland Eils, Oliver Strobel, Christian Conrad. ✉email: roland.eils@charite.de; oliver.strobel@meduniwien.ac.at; christian.conrad@charite.de

Pancreatic ductal adenocarcinoma (PDAC) is the most common pancreatic cancer type¹, with a current 5-year survival rate of just 9%², and is predicted to be the second leading cause of cancer mortality by 2030³. Only 10–20% of PDAC are resectable at diagnosis, and response to chemotherapy is generally poor although long-term survival is achieved in a small fraction of patients^{4,5}.

Large-scale genomic studies have identified recurrent genetic alterations in PDAC, with KRAS driver mutations detected in over 90% and inactivating mutations or deletions of TP53, SMAD4, and CDKN2A in over 50% of tumors^{6–9}. These alterations converge onto a limited number of aberrant signaling pathways^{10,11}. Metastatic lesions have been shown to share identical driver gene mutations with the primary tumor¹², further supporting a high level of genomic uniformity in PDAC. Defining the origins of clinical heterogeneity in PDAC to enable patient stratification and appropriate patient-specific treatment choices, therefore, remains a key challenge.

Transcriptomic analyses of PDAC have resulted in several subtype classification schemes^{11,13,14}, with most evidence supporting a distinction between ‘classical’ and ‘basal-like’ tumors¹⁵. The ‘classical’ subtype is associated with a higher level of mucinous features in histopathological assessment and longer survival¹⁴. Whether these subtypes reflect genetically distinct cells, different evolutionary pathways, or different progression status, remains unclear.

Whereas most earlier studies of transcriptional features of human PDAC were limited to a single sample per patient, recent RNA sequencing data from multi-region-sampled biopsies or even single tumor cells demonstrate a previously unappreciated degree of intratumoral heterogeneity in PDAC. In particular, transcriptionally and histologically defined subpopulations exhibiting ‘classical’ or ‘basal-like’ features were found to coexist in metastases from the same patient or even within the same tumor sample¹⁶. Furthermore, evidence from multi-region-sampled metastatic pancreatic cancers suggests that basal-like cell populations may emerge as a subclonal population within classical PDAC tumors¹⁷.

Regardless of sampling resolution, attempts to delineate transcriptional tumor subtypes or distinct functional cell types in primary PDAC are often confounded by differences in neoplastic cellularity, resulting in the erroneous inclusion of transcriptional features present in stromal or normal pancreas cells¹⁸. Differences in cell-type composition were also described in recent single-cell RNA sequencing (scRNA-seq) efforts, which identified distinct populations of cells within surgically resected PDAC; these include immune cells, fibroblasts, and endothelial cells as well as abnormal and malignant ductal cells^{19,20}. To simplify the study of PDAC tumor cells, patient-derived organoid models of human PDAC were introduced within the past five years, which reflect histopathologic, proteomic, genomic, and transcriptomic features of the original tumors yet remain experimentally tractable^{21–23}. Such models offer great potential for detailed analyses of PDAC biology and developing therapeutic approaches.

To investigate the functional identity and hierarchical relationships of PDAC cells, we here performed scRNA-seq of PDAC organoids of primary tumors and metastatic samples from 18 patients. We show that ‘classical’ and ‘basal-like’ cells may coexist within the same sample, and the level of subtype heterogeneity is linked to tumor grade. Despite transcriptional differences between tumors, patient-derived organoids share functional tumor cell states that are connected by a differentiation hierarchy also present in primary PDAC samples. Our results support the use of PDAC organoids to model tumor heterogeneity *in vitro*.

Results

PDAC organoids comprise malignant ductal cells. To enable the *in vitro* study of human PDAC, we derived 24 tumor

organoid lines from samples taken during surgery. Eighteen samples were obtained from primary tumors from individual patients. In one case, distinct organoid lines were derived from two pancreatic sites within the same primary tumor, providing a biological replicate (p080 and p081), and in another case, a technical replicate was generated by analyzing one organoid line at different passage numbers (p039 and p039b). We also obtained samples of two different liver metastases in addition to the pancreatic primary tumor from one patient (p083, p084 and p085), and two samples from unmatched metastases (Supplementary Table 1 and Fig. 1a, b). All tumors were classified as PDAC based on histological assessment. Patient-derived PDAC organoids, as well as nine of the biopsy samples, were classified based on bulk RNA sequencing as either basal-like or classical PDAC according to the subtypes defined by Moffitt et al.¹⁴; in each case, the PDAC organoid subtype corresponded to the biopsy sample subtype (‘Methods’ and Supplementary Table 1).

Single-cell RNA sequencing of all 24 tumor organoid lines resulted in transcriptomic information for a total of 93,096 cells after quality control, with a median of 3,877 cells from each organoid line and a median of 4,162 genes detected per cell (‘Methods’ and Supplementary Fig. 1a).

To determine the cell type identity of PDAC organoid cells, we compared single-cell transcriptomes from PDAC organoids with recent data from primary PDAC¹⁹. Across all patients, PDAC organoid cells were uniformly identified as malignant ductal cells by reciprocal principal component analysis and expression of characteristic genes (Supplementary Fig. 1b), consistent with previous observations that the *in vitro* culture conditions promote ductal cell growth²¹.

PDAC organoids show patient-specific gene expression. PDAC is characterized by a small number of recurrent genetic alterations that occur at high frequency, and therefore cannot account fully for differences in disease progression and therapeutic response between patients⁹. To investigate distinguishing features of PDAC organoids at the transcriptional level, we constructed a shared nearest neighbor (SNN) graph of all cells and found that cells from the same patient clustered together (Fig. 1c), even if they derived from different biopsies or metastatic sites processed separately. This indicates that transcriptional differences between patients are larger than within patients and are not merely due to technical batch effects. Patient-specific differences in transcriptional profiles were also not explained by individual known expression quantitative trait loci²⁴ (Supplementary Fig. 1c).

To further investigate the origin of transcriptional heterogeneity between PDAC tumors, we determined genes that were differentially expressed in organoid models of primary tumor cells derived from each patient compared to all others. While expression of the most highly upregulated genes in each PDAC organoid was often patient-specific (Fig. 1d, e and Supplementary Table 2), we observed that many of these genes belonged to the same gene families. Analysis of gene family membership of the top 20 enriched genes for each patient, excluding gene families defined by specific molecular domains, showed that the most highly represented gene families included cell surface and transmembrane proteins (CD molecules, claudins, and solute carriers), secreted proteins that interact with the extracellular matrix (mucins, kallikreins), enzymes that metabolize a range of substrates and potential drug targets (serine proteases, aldo-keto reductases), and type-I keratins (Fig. 1f). In PDAC organoids where these genes were detected, they were frequently expressed in a large proportion of cells, but with very low or zero expression in other lines (Fig. 1g). Since many of the gene families we identified have previously been proposed as indicators of tumor

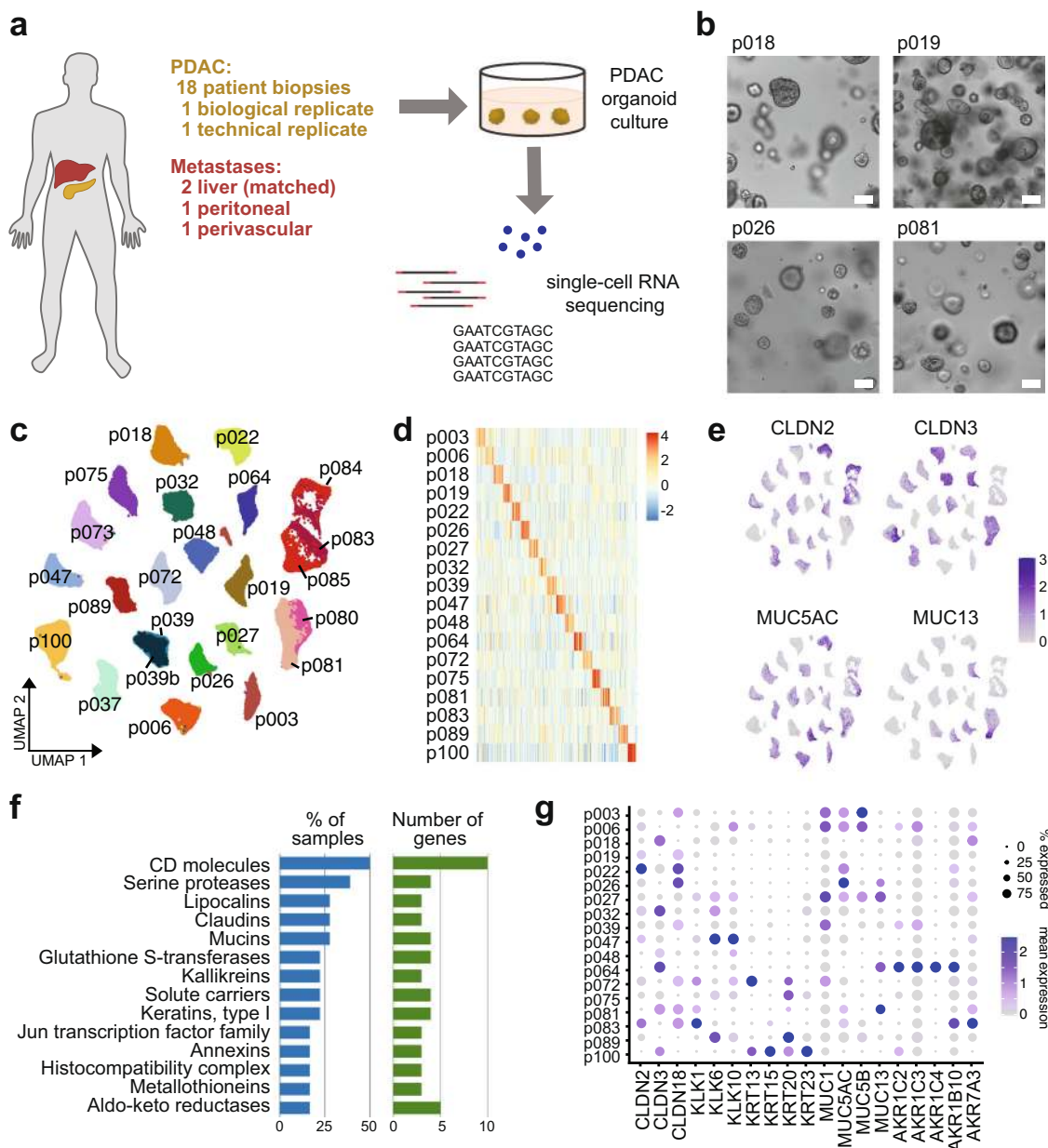


Fig. 1 Intertumor heterogeneity in patient-derived PDAC organoids. **a** Schematic of the experimental workflow. **b** Example images of four patient-derived PDAC organoid lines after 10 days of culture. Scale bars, 100 μ m. **c** UMAP embedding of 24 scRNA-seq samples from 18 patients, showing that cells cluster by patient origin (p039 is a technical replicate of p039b; p080 is a biological replicate of p081; p084 and p085 derive from liver metastases matched to p083). **d** Heatmap showing the expression of the 20 most highly differentially expressed genes per patient. **e** Expression of selected patient-specific genes, using the same UMAP representation as in **(c)**. **f** Gene group analysis of the 20 most highly differentially expressed genes per patient. Bar plots show the proportion of patients in which the indicated gene groups were overrepresented (blue), and the number of unique genes from each gene group (green). **g** Expression of selected patient-specific genes across all patients.

identity and/or prognosis in PDAC patients^{25–30}, these results have important implications for biomarker identification in PDAC, highlighting that samples from a large enough cohort of patients need to be analyzed in order to overcome interpatient transcriptional heterogeneity.

Subtype heterogeneity correlates with poor prognosis. PDAC is commonly classified into ‘classical’ and ‘basal-like’ transcriptional subtypes, with the latter carrying a poorer prognosis¹⁴. Bulk RNA-seq of PDAC organoids from our cohort grouped organoid lines into basal-like, classical, and intermediate subtypes (Supplementary Table 1). To elucidate subtypes at the single-cell level,

cells from all patient-derived organoids were scored for the expression of published subtype signatures consisting of 25 genes per subtype¹⁴. Overall, subtype annotation correlated well with bulk results (Supplementary Table 3). For the majority of patient-derived organoids, following PCA-based clustering of cells, subtype signature scores were homogeneous across cell clusters and reflected the subtype determined by bulk RNA-seq (Fig. 2a). Conversely, we identified a subset of patient-derived organoids containing both ‘basal-like’ and ‘classical’ cells (Fig. 2b), with corresponding marker gene expression (Fig. 2c). Notably, we found that PDAC organoids exhibiting heterogeneous subtype identity had been classified as WHO grade 3 or 4 tumors in histopathological assessments, whereas PDAC organoids with

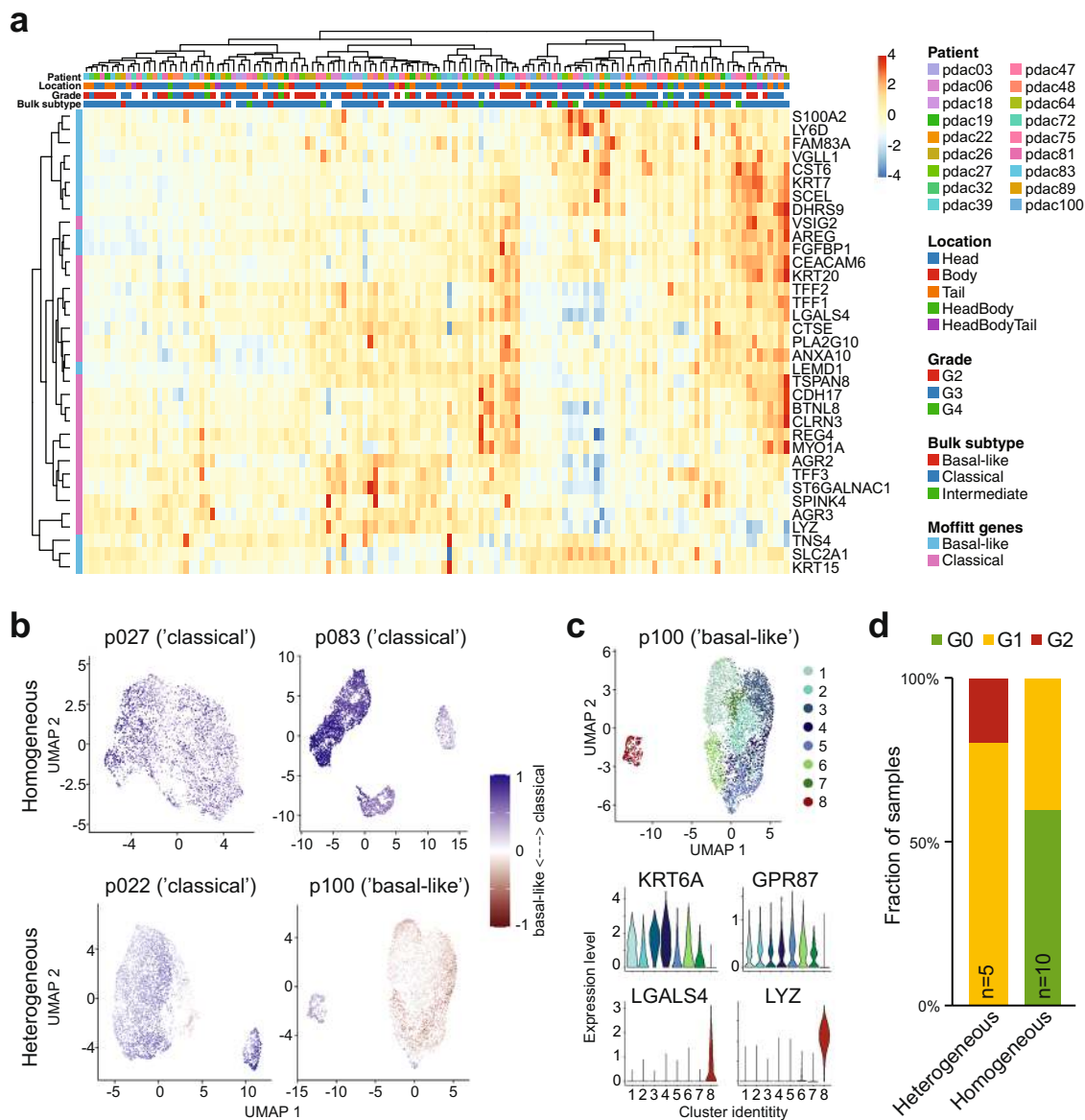


Fig. 2 Expression of PDAC subtype signatures. **a** Heatmap showing the expression of Moffitt subtype signature genes across individual clusters from all patients. **b** Distribution of Moffitt subtype scores across PDAC organoid cells, shown for two homogeneous (top) and two heterogeneous (bottom) samples. Blue indicates classical subtype scores, red basal-like (“Methods”). **c** Top: eight distinct clusters of cells were identified in p100. Bottom: expression of characteristic genes for the basal-like (top) and classical (bottom) subtype across clusters, showing significantly higher expression of classical genes and lower expression of basal-like genes in cluster 8 compared to all others. **d** Proportion of homogeneous and heterogeneous organoids that were classified as grade 2, 3, or 4 by histopathological assessment of the original tumor.

homogeneous subtype identity had been classified as grade 2 or 3 (Fig. 2d). Moreover, patients in our cohort with homogeneous classical PDAC tended to have longer overall survival whereas the outcome of basal-like tumors tended to be poorest (Supplementary Fig. 1d). Homogeneous enrichment for ‘classical’ subtype marker genes in PDAC organoid lines, therefore, correlates with more differentiated tumors, which are associated with a better prognosis.

Functional cell states are shared across patients. To identify cellular states that are shared across tumors, we performed reciprocal PCA-based integration of 18 primary PDAC organoid transcriptomes (“Methods”). Clustering of cells revealed nine functional cell states that were conserved across patients (Fig. 3a and Supplementary Fig. 2a).

We evaluated the characteristics of each cluster by differential expression analysis (Fig. 3b and Supplementary Table 4). Five clusters represented cell moving through the different cell cycle phases (labeled Cycling-1 to Cycling-5). Two clusters were devoid of cycling cells (labeled Noncycling-1 and Noncycling-2), but comprised cells expressing cyclin-dependent kinase inhibitor 1 (Supplementary Fig. 3a). These clusters showed increased expression of genes involved in secretion, digestion, cell adhesion, and locomotion. While immune response signaling was generally upregulated across the noncycling clusters, one additional cluster (labeled IFN-1) showed specific expression of genes involved in type I interferon signaling. The smallest cluster (labeled CXC-1) was enriched for cells expressing CXC motif ligands such as *CXCL1*, *CXCL2*, and *CXCL8*, which are thought to stimulate cancer cell proliferation and migration^{31–33}. Clusters IFN-1 and CXC-1 both comprised cycling and quiescent cells

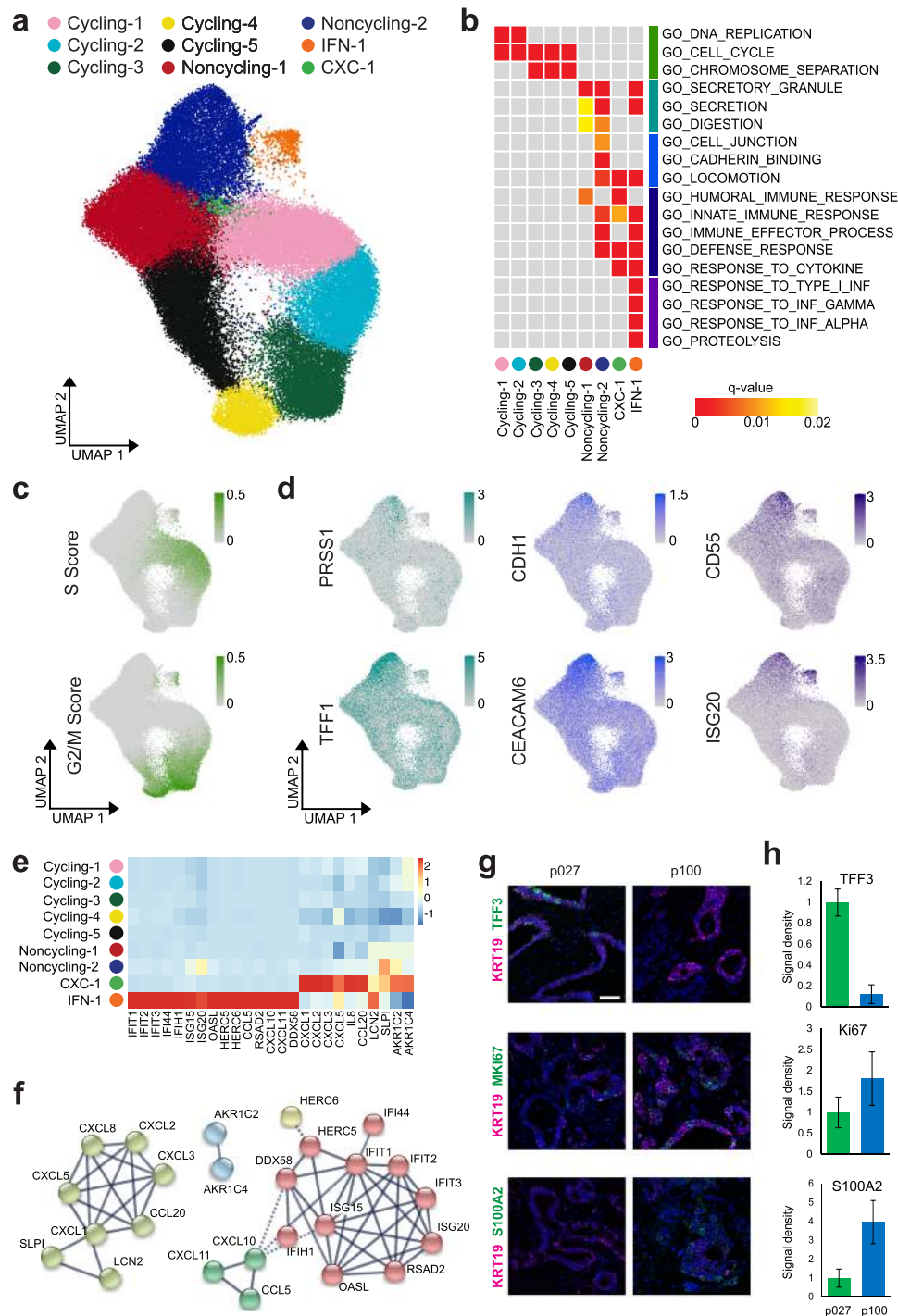


Fig. 3 Functional cell states shared across PDAC patients. **a** UMAP representation of clusters shared across patients, after PCA-based integration of PDAC transcriptomes from 18 primary PDAC organoid lines. **b** Gene ontology (GO) term enrichment analysis using the top 100 upregulated genes per cluster. Gray boxes indicate no significant enrichment. **c** Cell cycle scores for each cell, computed based on the expression of S and G2/M phase genes, were visualized using the same UMAP representation as in **(a)**. **d** Expression of characteristic genes across all cells from primary PDAC organoid lines, visualized using the same UMAP representation as in **(a)**. **e** The heatmap shows the average expression per cluster of genes specifically enriched in clusters CXC-1 and IFN-1 with interactions recorded in the STRING database⁵⁵. **f** Networks representing gene interactions considered in **(e)**. **g** Representative images of RNA fluorescence in situ hybridization (FISH) staining for KRT19 indicating PDAC cells (magenta) together with either TFF3, MKI67, or S100A2 (green) in primary tumor sections from p027 and p100. Nuclei are stained with DAPI (blue). Scale bar, 50 μ m. FISH staining was repeated twice on individual sections with similar results. **h** Quantification of RNA FISH stainings shows the signal density per nucleus for each transcript in PDAC cells (identified by KRT19 staining), normalized to the density in sample p027 (p027: $n = 339$ nuclei for MKI67 and TFF3, 369 nuclei for S100A2; p100: $n = 176$ nuclei for MKI67 and TFF3, 306 nuclei for S100A2; each from three separate images, with error bars showing standard errors in the mean).

(Supplementary Fig. 3b). Notably, the cycling and noncycling clusters contained cells from all patient samples, but only five patients (p006, p018, p027, p047, and p089) contributed at least 1% of sampled cells to cluster IFN-1 and only two patients (p064 and p100) contributed similarly to cluster CXC-1 (Supplementary Table 5). RNA in situ hybridization confirmed the differential representation of clusters IFN-1 and CXC-1 in patient-derived cultures as well as primary tumors (Supplementary Fig. 2b).

We thus concluded that all patient-derived PDAC organoids contained cycling cells, which we resolved into different cell cycle phases (Fig. 3c), and differentiating cells assuming functional characteristics reminiscent of their pancreatic origin (Fig. 3d). In addition, a subset of patients also harbored cell clusters with specific expression of cytokines thought to contribute to tumor progression by autocrine and paracrine mechanisms (Fig. 3e, f).

RNA in situ hybridization of surgical primary tumor samples for KRT19 (a marker of neoplastic PDAC cells), TFF3 (a marker of secretory cells and of the classical PDAC subtype), S100A2 (a marker of the basal-like PDAC subtype), and MKI67 (a proliferation marker) showed higher TFF3 expression in the classical subtype and higher S100A2 expression in the basal-like subtype (Fig. 3g, h), confirming that PDAC organoids reflect the original patient tumors.

Differentiation hierarchy in PDAC organoids. Based on the observation that a subset of clusters shared across PDAC organoid lines contained cycling cells, we sought to identify the differentiation trajectory of PDAC organoid cells. Applying the recent concept of RNA velocity³⁴, we determined changes over time in gene expression, as estimated by the relative abundance of unspliced and spliced mRNA in each sample (Fig. 4a). By Markov chain tracing, we identified probable startpoints and endpoints of differentiation trajectories (Fig. 4b). Across all patients, trajectory startpoints coincided with cycling clusters, with most trajectories converging onto cluster Cycling-4 as the cell population of origin (Fig. 4b, c). Trajectory endpoints, on the other hand, were predominantly located in the distant cluster Noncycling-2 (Fig. 4b, c).

Notably, when relating the Moffitt subtype identity of cells to their position along the lineage trajectory, we found that the ‘classical’ gene signature was enriched in the differentiated secretory compared to the cycling cells (Fig. 4d, e).

As our in vitro organoid model is enriched for progenitor-like cells compared to primary tumor samples (Supplementary Fig. 1b), different cell cycle phases could be resolved in our data, and we identified a bifurcation point in G1 phase at which cells either re-enter the cell cycle or differentiate towards the secretory state (Fig. 4f). To further investigate the fate behavior of PDAC organoid cells, we calculated a minimum spanning tree linking all cells in clusters Cycling-1, Cycling-5, Noncycling-1, and Noncycling-2, and assigned each cell a pseudotime value along the bifurcating path. In addition to ubiquitous cell cycle-related genes, this approach identified potential drivers of cellular fate; for example, *GGCT* (gamma-glutamylcyclotransferase) and *RANBP1* (Ran-binding protein 1) show increased expression soon after the bifurcation point in cells re-entering the cell cycle, whereas the cell adhesion gene *CEACAM6* and *S100A6* encoding a calcium-binding protein are upregulated in differentiating cells (Fig. 4g).

We thus conclude that PDAC organoid growth is fueled by a large pool of cycling cells, which sustain a population of differentiating progeny that assume secretory function. Notably, this functional hierarchy is conserved in PDAC organoids from all patients in our cohort, as well as in scRNA-seq data from primary PDAC (Supplementary Fig. 2c).

Liver metastases re-establish aspects of the primary tumor. PDAC is frequently metastatic at diagnosis, with only 10–20% of patients qualifying for a potentially curative surgery³⁵. While most patients with advanced PDAC receive palliative chemotherapy, the benefit of neoadjuvant chemotherapy is a subject of current debate^{36,37}. A recent bulk whole-genome sequencing study of treatment-naïve PDAC tumors and metastatic lesions found identical known driver gene mutations in primary tumors and all matched metastases¹², spurring hope that targeted therapies could therefore provide a clinical benefit in advanced PDAC by simultaneously eliminating genetically homogeneous cells at multiple sites.

Here, we addressed the question of cellular heterogeneity in metastatic PDAC at the transcriptional level, by deriving PDAC organoid lines from two liver metastases (M1 and M2) and from the same patient’s primary tumor (P). After merging single-cell transcriptome data from the three samples by reciprocal PCA, we identified five cell clusters with differential representation in the three PDAC organoid lines (Fig. 5a). All samples contained cycling cells, as indicated by *MKI67* expression (Fig. 5b). Other functional aspects of PDAC, including secretion (e.g., *FABP1*, *SCG5*), digestive enzymes (e.g., *PRSS1*, *PGC*), cytoskeleton or cell adhesion genes (e.g., *ANXA6*, *TUBB2B*, and *CEACAM6*), MHC complex members (e.g., *CD74*, *HLA-DQB1*, and *HLA-DRB1*) and putative inflammasome inhibitory genes (e.g., *TMEM176A*, *TMEM176B*)³⁸, were heterogeneously expressed between clusters (Fig. 5c). For example, cluster 2, which was enriched for genes related to secretion and digestion, was detected in P and M2, but not in M1.

Bulk RNA-seq suggested that both metastasis-derived organoid lines showed more ‘basal-like’ gene expression than organoid lines derived from the primary tumor (Supplementary Table 1), consistent with earlier observations of ‘basal-like’ phenotype enrichment in metastatic tissues¹⁴. Conversely, at the single-cell level, we found transcriptional subtype heterogeneity even within a single metastasis-derived organoid line, with a subset of cells from M2 showing more ‘classical’ gene expression than a subset of cells derived from the primary tumor (Fig. 5d).

By projecting scRNA-seq data from both metastasis-derived organoid lines onto the PCA of all primary PDAC organoid transcriptomes, we further observed a depletion of differentiated cells (cluster ‘Noncycling-2’) especially in M1 (Fig. 5e), corresponding to the depletion of functional cluster 2 identified above (Supplementary Fig. 3c).

These observations suggest that metastatic PDAC lesions in the liver re-build diverse aspects of the original tumor, including the differentiation hierarchy identified in primary samples. Since both M1 and M2 express genes also detected in the primary tumor but not shared between the metastases, the observed gene expression pattern is consistent with an underlying homogeneous mutational landscape in combination with differential epigenetic control, possibly driven by the local microenvironment or chance events. While PDAC metastases thus appear more heterogeneous at the transcriptional compared to the genomic level¹², differences in gene expression may not be the result of de novo events, with encouraging implications for future targeted therapies.

PDAC organoids provide an in vitro model for drug screens. In the quest to develop novel chemotherapies for PDAC patients with advanced metastatic disease or unfavorable transcriptional subtypes, organoid models offer great potential for in vitro drug response screens. To illustrate the utility of our PDAC organoid lines for screening applications, we applied a recent automated microscopy-based live-cell assay and quantification workflow (*DeathPro*)³⁹. In this workflow, all cells are stained with Hoechst

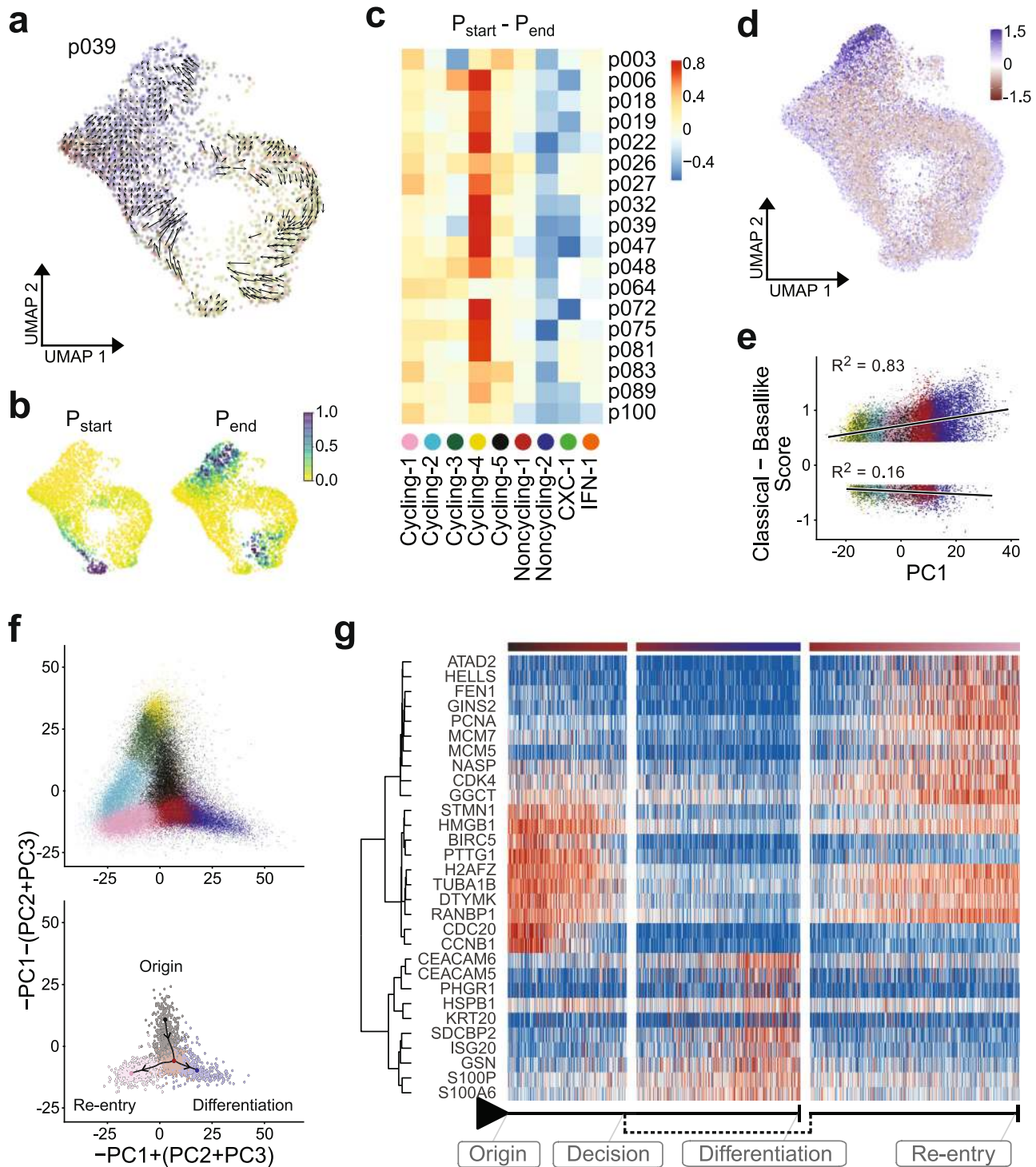


Fig. 4 Differentiation hierarchy of PDAC cell states in vitro and in vivo. **a** RNA velocity trajectory shown for p039, using the same UMAP representation as in Fig. 3a. **b** Startpoint (top) and endpoint (bottom) probabilities shown for p039. **c** Difference between the average startpoint (red) and endpoint (blue) probabilities within each cluster (columns) across all PDAC organoid samples (rows). **d** Distribution of PDAC subtypes in single cells along the lineage trajectory. Colors indicate whether a cell exhibits higher expression of ‘classical’ (blue) or ‘basal-like’ (red) subtype marker genes. **e** Correlation of PDAC subtype scores with cell embeddings in the first principal component, which distinguishes cycling cells (negative values in PC1) from differentiating cells (positive values in PC1). **f** Projection of all cells onto a linear combination of PC1, PC2, and PC3 to visualize cycling and differentiating cells (top). Cells in the four clusters around the trajectory bifurcation point were linked by a minimum spanning tree (bottom). **g** Expression of genes with dynamic changes along the bifurcation branches (red: high, blue: low), with hierarchical clustering of gene expression shown on the left. Column annotations indicate position along the branches.

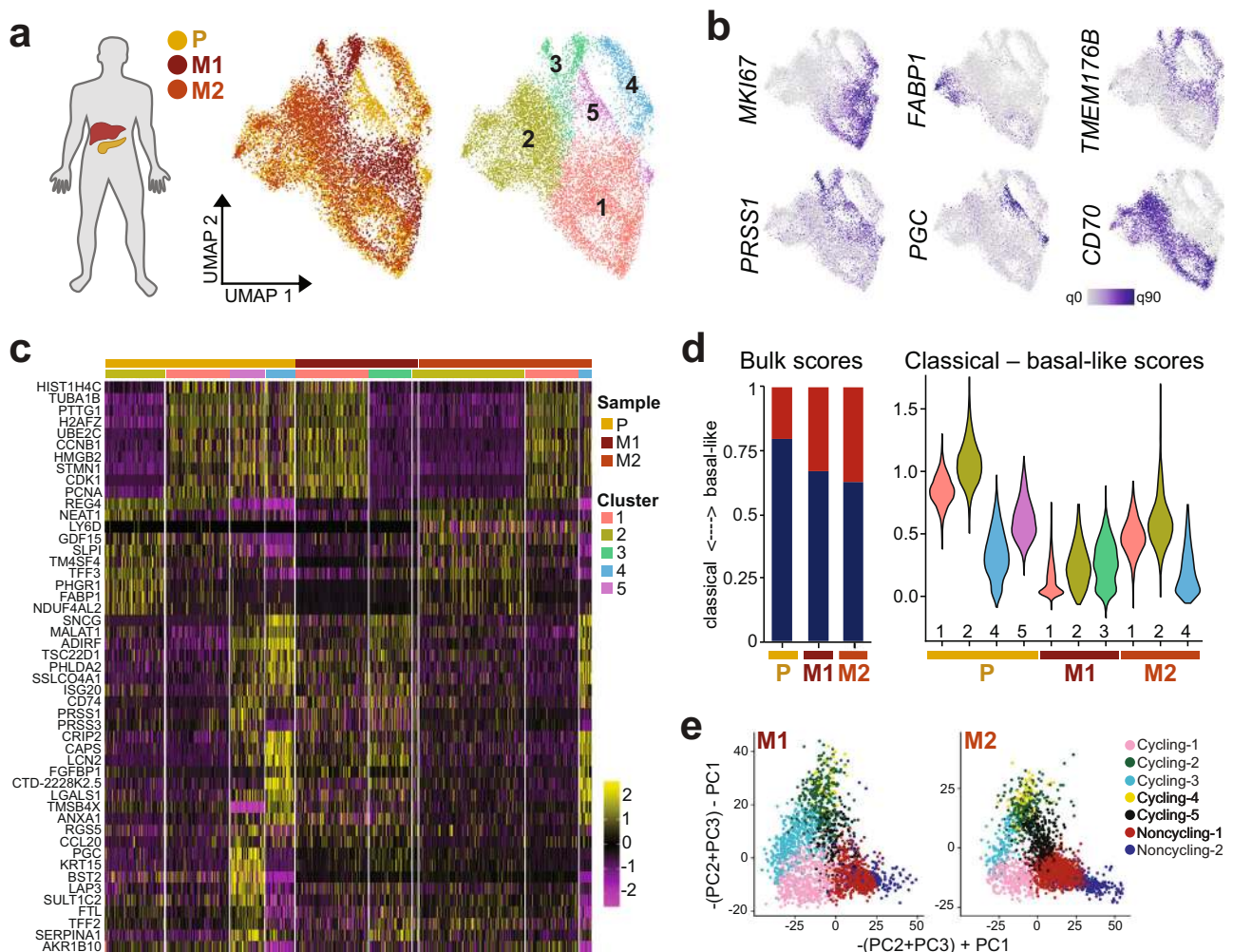


Fig. 5 Functional and transcriptional subtype heterogeneity in liver metastases. **a** For one patient, organoid lines were derived from the primary tumor (P) as well as two liver metastases (M1 and M2). Shown is a UMAP representation of transcriptomes integrated by reciprocal PCA, with shared and organoid line-specific cell clusters identified by unsupervised clustering. Cells are colored by sample origin (left) and cluster membership (right). **b** Expression of genes involved in cell cycle (*MKI67*), secretion and digestion (*FABP1*, *PRSS1*, and *PGC*), and immune regulation (*CD70*, *TMEM176B*) across cells from P, M1, and M2 organoids. **c** Expression of the top 10 enriched genes for each cluster. **d** Moffitt subtype scores from bulk RNA-seq data (left) and single-cell RNA-seq data (right) for P, M1, and M2 organoids. Blue indicates classical subtype scores, red basal-like (“Methods”). Cells are grouped by cluster identity according to (a) in the violin plots. **e** Projection of M1 and M2 transcriptomes onto the primary PDAC organoid data (see Fig. 4f and “Methods”) shows the distribution of cells across cycling and differentiating clusters.

33342 and propidium iodide (PI) to distinguish live and dead cells; the total areas covered by dead cells (PI) and all cells (Hoechst 33342 or PI stained) are then measured from projected confocal images and used to calculate area-under-curve values for cell death (AUCd) and proliferation inhibition (AUC_{pi}). Compared to simpler luminescent cell viability assays, this approach resolves drug-induced cell death and proliferation inhibition³⁹. Here, we measured PDAC organoid cell death and proliferation inhibition induced by six drugs in clinical use for PDAC therapy; these were 5-FU, Gemcitabine, Irinotecan, Paclitaxel, Erlotinib, and Oxaliplatin (Fig. 6a and Supplementary Table 6).

5-FU and Gemcitabine elicited the most cell death and proliferation inhibition across all organoid lines included in the screen, with Erlotinib and Oxaliplatin the least effective, although significant heterogeneity in drug responses was observed between organoid lines (Supplementary Fig. 4a). For each drug, ‘classical’ subtype gene expression was correlated with more pronounced proliferation inhibition in response to drug treatment, whereas drug-induced cell death showed less correlation with PDAC subtype (Fig. 6b and Supplementary Fig. 4b).

Taken together, our results indicate that the ‘classical’ subtype signature is linked to better drug responses and a higher level of differentiation, while the ‘basal-like’ signature with poorer prognosis is linked to cell proliferation and reduced drug responses (Fig. 6c and Supplementary Fig. 4c).

Discussion

PDAC remains a challenging entity for experimental study; ex vivo tumor samples are difficult to access and often have low malignant cell content¹⁵. Recent advances in in vitro organoid technologies have therefore sparked hope for an alternative route. We have shown here that PDAC organoids established with our protocol are transcriptionally equivalent to malignant ductal cells. Notably, our results strongly overlap with previously published primary PDAC scRNA-seq data¹⁹, suggesting that PDAC organoid cells recapitulate key aspects of cell state heterogeneity in the malignant ductal cell compartment in vitro. They are also consistent with a recent scRNA-seq study highlighting substantial intratumor heterogeneity in human primary PDAC tumors⁴⁰.

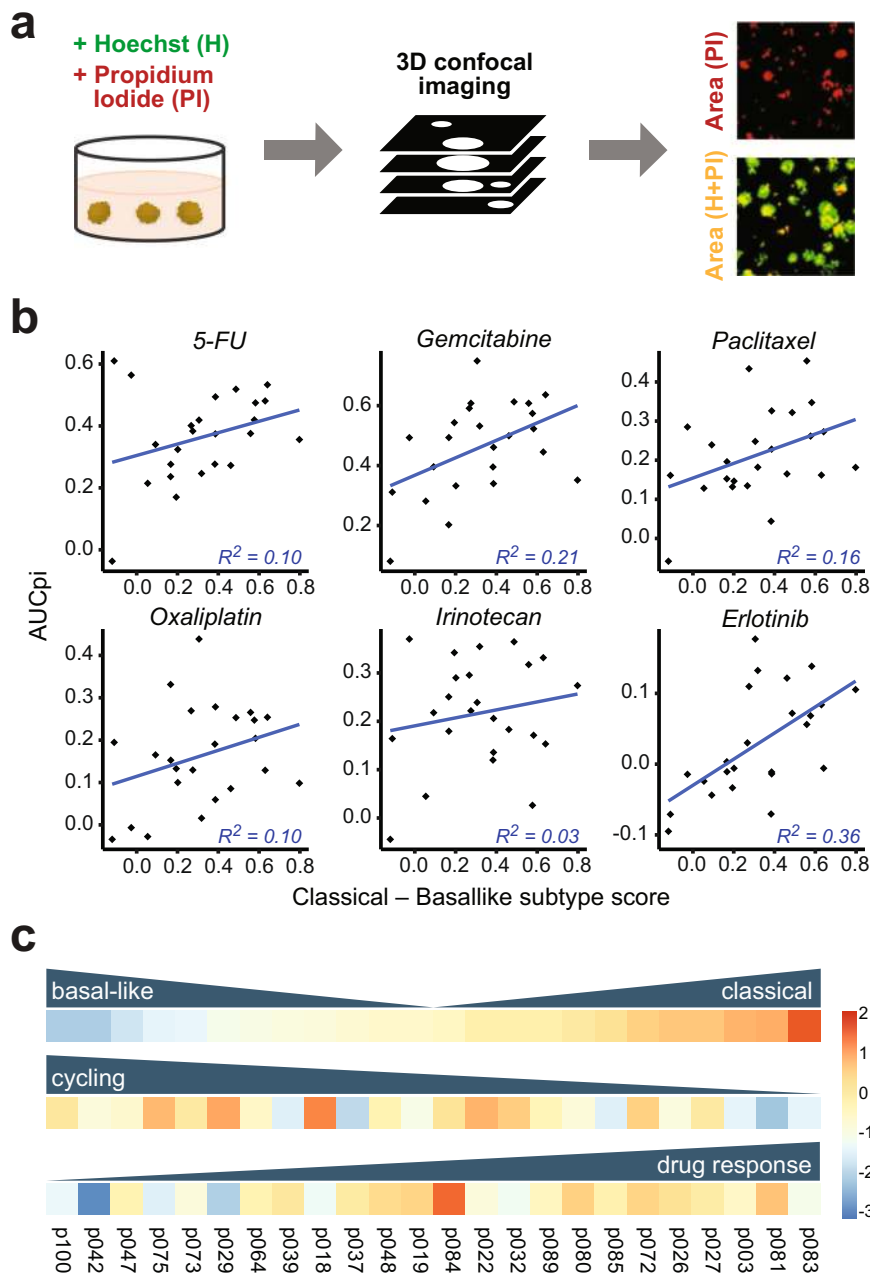


Fig. 6 Classical subtype gene expression correlates with organoid drug responses. **a** Overview of the experimental drug screen protocol. PDAC organoids were treated with a range of drug concentrations over 72 h, and then subjected to 3D confocal imaging. By measuring the intensity of Hoechst (H) and propidium iodide (PI) signals, scores were computed to compare drug-induced cell death and proliferation inhibition. Scale bars, 200 μ m. **b** Correlation between median subtype scores calculated from scRNA-seq data and drug-induced proliferation inhibition, as measured by the area under curve (AUCpi), for 24 PDAC organoid lines. A higher score on the x-axis represents a more ‘classical’ transcriptional phenotype. **c** Overview of variation in transcriptomic PDAC subtype (top), median cell cycle score (middle), and proliferation inhibition in response to 5-FU treatment (bottom), shown as z-scores scaled across all samples.

By deriving primary PDAC organoids from 18 patients, we found that PDAC organoids show patient-specific differences that mask the shared cell state heterogeneity we also identified. This observation highlights the need to include a sufficiently large number of patient samples in single-cell studies in order to distinguish common features from individual variation, enabling extrapolation to a larger patient collective. We observed frequent differential expression of genes encoding cell surface and secreted proteins between patients, often from the same gene families (e.g., claudins, mucins). These transcriptional differences may thus not always have functional relevance, but could reflect underlying

genetic or epigenetic heterogeneity, different cells of origin or microenvironments of the tumor, lifestyle and comorbidities of the patient, or differences in therapy and immune response. It will be interesting to explore the origin of patient-specific transcriptome profiles in future studies and determine if this heterogeneity is also present in healthy pancreas cells or arises during tumorigenesis.

To categorize transcriptional heterogeneity in PDAC, an established classification scheme distinguishes ‘classical’ from ‘basal-like’ tumors. In line with recent results from other groups^{17,41}, our cohort comprised PDAC organoids with

uniformly ‘classical’ gene expression, but also a subset of organoids with heterogeneous expression of subtype marker genes across cells. The latter was associated with a poorer prognosis of the patient, as determined by histopathological grading of the original tumor and patient outcomes. As our cohort did not include any tumors that were purely ‘basal-like’, it was impossible to resolve whether poorer prognosis simply results from higher ‘basal-like’ cell content or whether the extent of subtype heterogeneity is an independent predictor, which thus remains an interesting question for future studies. It should also be noted that the relative paucity of basal-like cells in our PDAC organoids may reflect selective pressure exerted by the *in vitro* culture conditions towards ‘classical’ subtype gene expression, which represents an emerging limitation of PDAC organoids⁴². Nevertheless, the broad agreement of organoid subtype assignments with original tumor subtypes indicates that differences between PDAC samples are retained in culture, consistent with an earlier study in which PDAC organoid drug responses paralleled patient outcomes⁴³.

Despite substantial interpatient heterogeneity, our results identified functional cell states that are shared across patients, and are linked by a differentiation hierarchy conserved *in vitro* and *in vivo*. Proliferating cells may either re-enter the cell cycle, or give rise to differentiating cells that acquire characteristics of pancreatic tissue including digestive and secretory functions. Expression of genes involved in digestion and secretion has previously also been observed in primary PDAC, again confirming that our organoid model captures key aspects of this entity⁴⁴. While our analyses provide initial insight into differential gene expression at the bifurcation point, future studies should address whether the fate choice of tumor cells could be exogenously biased towards differentiation in order to constrain tumor growth. In addition, it will be interesting to investigate whether a subset of cells in clusters ‘Noncycling-1’ and ‘Noncycling-2’ may be able to re-enter the cell cycle, which would enhance the growth potential of the tumor.

Importantly, malignant cells may express a combination of transcriptional programmes that are not normally found within the same cell type in the healthy pancreas. By comparing scRNA-seq data from organoid lines derived from two liver metastases to the matched primary tumor, we also found that metastases may activate different combinations of pancreatic transcriptional programmes. As PDAC metastases are known to share the same driver mutations as the primary tumor¹², heterogeneity in PDAC metastases therefore most likely arises from differential epigenetic regulation activating or deactivating transcriptional programmes.

The expression of pancreatic programmes in liver metastases of PDAC also resolves a debate regarding the role of normal pancreas genes in PDAC transcriptome data. Due to the frequently low tumor cellularity of PDAC, it has been questioned whether genes that are normally expressed in mature pancreatic tissue should be excluded from analyses of PDAC pathophysiology, assuming that they represent normal tissue contamination¹⁸. Not surprisingly, a recent study found an association between the presence of normal pancreatic transcripts and the presence of healthy tissue contamination on PDAC tumor slides⁴⁵. Our results indicate that such genes may in fact be expressed by malignant cells in PDAC tumors, even in distant metastatic lesions, and their inclusion in future studies of PDAC pathophysiology is therefore warranted.

In addition to proliferating cells and differentiating cells with pancreatic expression programmes, a subset of PDAC organoid lines contained distinct clusters of cells that may mediate type I interferon signaling (cluster IFN-1) or CXC motif cytokine signaling (cluster CXC-1). As these signaling pathways have been implicated in cancer progression and metastasis as well as therapy responses^{31–33,46}, resolving the presence of corresponding cell

populations by single-cell transcriptome studies could improve prognostic accuracy for patients in the future.

Our drug screen showed that drug response, both at the level of cell death and proliferation inhibition, was positively correlated with the expression of ‘classical’ subtype genes, and negatively correlated with ‘basal-like’ gene expression. PDAC organoid lines with higher drug response also tended to display a more differentiated transcriptome, whereas lower drug response was associated with higher cell cycle scores. These results are consistent with ‘basal-like’ PDAC tumors showing poorer response to standard therapy and worse prognosis in the clinic. In particular, a recent study suggests that FOLFIRINOX combination chemotherapy induces a shift towards a more ‘basal-like’ state in PDAC cell lines and patient tumors⁴⁷, suggesting that ‘basal-like’ cells may be intrinsically more resistant to chemotherapy or selected for as an adaptive response. Our organoid-based assay represents a promising approach for the *in vitro* identification of compounds that could improve therapeutic outcomes for PDAC patients in a subtype-dependent manner.

Methods

PDAC organoid generation and maintenance. Pancreatic tumor organoid cultures were established using an adaptation of the previously described protocol²¹. Pancreatic tumor specimens were obtained from patients undergoing surgical resection at the Surgical Department of the Heidelberg University Hospital following approval by the Ethics Committee of Heidelberg University (ethic votes 301/2001, 159/2002, S-206/2011, S-708/2019). Written informed consent from all patients was obtained prior to acquisition of tissue. Tumor specimens were minced and digested for up to 4 h at 37 °C in AdMEM/F12 medium (Gibco) containing 2 mM GlutaMAX (Gibco), 10 mM HEPES (Gibco), 1× Primocin (InvivoGen), 1 mg/ml Collagenase type IV (Sigma-Aldrich), 100 µg/ml DNase I (AppliChem), 1× B27 (Gibco), 1 mM N-acetylcysteine (Sigma-Aldrich) and 10 µM Y-27632 (Selleckchem). Dissociated cells were seeded in Growth Factor Reduced Matrigel (Corning) and cultured in growth organoid medium consisting of AdMEM/F12 medium, 2 mM GlutaMAX, 10 mM HEPES, 1× Primocin, 1× B27, 1 mM N-acetylcysteine, 10% RSPO1-conditioned medium⁴⁸, 100 ng/ml FGF10 (PeproTech), 100 ng/ml Noggin (PeproTech), 500 nM A83-01 (Tocris) and 10 µM Y-27632. The medium was refreshed every 3–4 days omitting Y-27632. Organoids were routinely passaged by dissociation with TrypLE (Gibco) for 10 min at 37 °C. The medium was further supplemented with 50 ng/ml EGF (PeproTech) and, if required, with 50% Wnt3A-conditioned medium⁴⁹ only after tumor cell enrichment to avoid overgrowth of normal ductal cells during the initial passages. PDAC organoids were cultured for 2.2 months on average before bulk RNA-seq (range: 1.0–4.7 months), and 3.6 months on average before scRNA-seq (range: 1.9–5.8 months). The technical replicates p039 and p039b were cultured for 2.8 months and 4.2 months, respectively, before scRNA-seq.

Single-cell dissociation and RNA sequencing. Single-cell sequencing libraries were prepared according to the 10x Genomics Single Cell 3 v2 Reagent Kit user guide with small modifications. Organoid cultures were expanded in growth medium without addition of Wnt3A-conditioned medium (serum-free condition) for 5 days and dissociated into single cells for 30–60 min using AccuMax (Invitrogen) supplemented with 0.3 mg/ml Dnase I. Cells were washed with PBS containing 0.04% BSA, strained through a 20 µm strainer (PluriSelect) and counted. Single-cell suspensions containing 10,000 cells were loaded following the protocol of the Chromium Single Cell 3’ Library Kit v2 (10x Genomics) to generate cell and gel bead emulsions. After droplet generation, samples were transferred onto a pre-chilled 96-well plate (Eppendorf), heat-sealed, and reverse transcription was performed using a Bio-Rad C1000 Thermal Cycler. After reverse transcription, cDNA was recovered using Recovery Agent followed by Silane DynaBead clean-up. Purified cDNA was amplified for 15 cycles and cleaned up using SPRIselect beads (Beckman). Samples were quantified on an Invitrogen Qubit 4 Fluorometer. cDNA libraries were prepared according to the Single Cell 3 Reagent Kits v2 guide with the appropriate choice of PCR cycle number based on the calculated cDNA concentration. Final libraries were sequenced in one lane per sample with the Illumina NextSeq 500 system in high-output mode (paired-end, 75 bp).

scRNA-seq data alignment and quality control. Raw sequencing data were processed using Cell Ranger version 2.1.1 (10x Genomics). Transcripts were aligned with the 10x reference human genome hg19 1.2.0. Quality control and downstream analysis were performed with Seurat version 3.0⁵⁰. Cells with fewer than 200 genes or genes represented in fewer than three cells were excluded from the analysis. Cells with >100,000 reads or >15% mitochondrial reads were excluded. Count data were log-normalized with a scale factor of 10,000, and the 2000 most variable genes

identified with the FindVariableFeatures function in Seurat. Normalized data were scaled using the ScaleData function.

Analysis of individual organoid samples. For the analysis of individual samples, organoid scRNA-seq data from primary tumors and metastases was processed with the Seurat package in R, using the FindClusters function with a resolution of 0.5. To identify differences between patients, expression data from all samples were combined and clustered using the FindClusters function with a resolution of 0.1, resulting in one cluster per organoid except for pdac100, for which we manually combined two resulting clusters. The dimensional reduction was performed using the uwot package version 0.1.5. Differentially expressed genes for primary PDAC samples were identified using a Wilcoxon rank-sum test. As p080 and p081 were derived from the same patient, only the latter was included in this analysis. The top 20 enriched genes per sample that were expressed in at least 25% of cells in this sample and at most 90% of cells in all others, were analyzed according to their gene group membership.

Moffitt subtype analysis. To analyze Moffitt subtypes, cells from each patient were clustered using the FindClusters function in Seurat with a resolution of 0.5. The average expression of 25 marker genes each for the 'classical' and 'basal-like' subtype¹⁴ was then determined for each cluster. The gene expression heatmap was generated using the complete clustering of Spearman correlation coefficients. Subtype scores for basal-like (S_{bas}) and classical (S_{cla}) marker gene expression for each individual cell were calculated using the AddModuleScore function in Seurat, and a combined score ($S_{moff} = \max[0, S_{cla}] - \max[0, S_{bas}]$) was calculated for each cell.

Joint analysis of PDAC samples by reciprocal PCA. To analyze cell states across patients, primary tumor samples were merged by reciprocal PCA. As p080 and p081 were derived from the same patient, only the latter was included in this analysis. Cells were clustered in Seurat using the FindClusters function with the Louvain algorithm with a resolution of 0.7, and dimensional reduction was performed using the umap-learn package version 0.3.10⁵¹. Differentially expressed genes for each cluster were identified using a Wilcoxon rank-sum test. Gene ontology (GO) term analysis was performed using the MSigDB version 7.1^{52,53} with the top 100 enriched genes per cluster with adjusted p -value < 0.05. One cluster resulted in only six enriched genes and no enriched GO terms but comprised cells with the highest number of RNA counts in the dataset, suggesting a technical artefact; it was therefore excluded from the analysis. Cell cycle scores were calculated with the AddModuleScore function in Seurat, using previously published lists of S phase and G2/M phase marker genes⁵⁴. We used the STRING database version 11⁵⁵ to identify gene interaction networks specifically expressed in clusters, with the confidence cut-off at 0.75 and k -means clustering with $k = 5$.

Comparison to primary PDAC scRNA-seq data. To compare scRNA-seq data from our PDAC organoids with primary PDAC, we downloaded raw data for two patients (T18 and T20) from a recent publication¹⁹. Primary PDAC data was processed analogously to PDAC organoid data, and dataset integration was performed using reciprocal PCA in Seurat, with primary PDAC as the reference. Cell type identification was based on established marker genes¹⁹.

Inference of a lineage hierarchy. We used the velocity Python package version 0.17.16³⁴ to estimate RNA velocities by distinguishing unspliced and spliced mRNAs. Correlations of S_{moff} with PC1, which resolved cycling from differentiated cells, were calculated by linear regression using mean values across cells within bins of equal width in both S_{moff} and PC1. For visualization, only cells with greater than median S_{moff} for $S_{mof} > 0$ or smaller than median S_{moff} for $S_{mof} < 0$ were plotted. Linear combinations of cell embeddings for the first three principal components, specifically $-PC1 + (PC2 + PC3)$ and $-PC1 - (PC2 + PC3)$, were chosen to illustrate the branching point at which cells either re-enter the cell cycle or differentiate. Following this two-dimensional projection, a randomly sampled subset of 3,000 cells in clusters Cycling-1, Cycling-5, Noncycling-1, and Noncycling-2 were located along a bifurcating trajectory by a minimum spanning tree. Expression of genes varying along the trajectory was visualized using the dynverse package version 0.1.1 in R⁵⁶. To determine if an equivalent trajectory could be resolved in vivo, two primary PDAC datasets (T18 and T20) from a recent publication¹⁹ were processed analogously.

Comparison of metastases to the primary tumor. To compare the transcriptome of PDAC organoids derived from two metastases (p084 and p085) to organoids derived from the corresponding primary tumor (p083), transcriptomes from these three samples were merged by reciprocal PCA, and cells were clustered with a resolution of 0.3. Expression of the top 10 upregulated genes for each cluster was visualized in a heatmap. Subtype scores were calculated as described above. For trajectory analysis, integrated gene expression data was projected onto the PCA of all primary tumor samples, using the first 50 principal components. Cluster identity of metastases-derived cells was determined according to their similarity to primary tumor-derived cells, using the TransferData function in Seurat.

RNA fluorescence in situ hybridization. Sections of PDAC organoids or primary tumor samples were processed for RNA in situ detection using the RNAscope Multiplex Fluorescent Reagent Kit v2 according to the manufacturer's instructions (Advanced Cell Diagnostics). RNA fluorescence in situ hybridization (FISH) images were acquired on a Leica SP8 confocal laser scanning microscope equipped with a 40x/1.30 oil objective (Leica HC APO CS2). Images were binarized, Gaussian filtering followed by watershed segmentation was applied to identify nuclei, and binarized FISH signal density per nucleus was calculated using ImageJ.

Imaging-based drug screen. The organoid-based drug screen was performed using the 'DeathPro' workflow as previously described³⁹ on a subset of 24 PDAC organoid lines, including one derived from an unmatched peritoneal metastasis (p073) and one derived from an unmatched perivascular metastasis (p037). Briefly, drugs were dissolved in DMSO, water, PBS, or ethanol as required and stored as single-use aliquots at -80°C . Drug dilution series (1:3) were prepared in PDAC organoid culture medium containing 1 $\mu\text{g}/\text{ml}$ Hoechst (Invitrogen) and 1 $\mu\text{g}/\text{ml}$ PI (Sigma). Organoids were incubated in Matrigel-coated 96-well Angiogenesis μ -Plates (ibidi) with drug-containing medium for 72 h. Organoid cultures were then washed twice with PBS and the medium was exchanged for a drug-free medium. Cells were imaged 72 h after the start of drug treatment using a Zeiss LSM780 confocal microscope, 10x objective (EC Plan-Neofluar 10x/0.30 M27), and 405 and 561 nm diode lasers in simultaneous mode. Imaging was performed in an incubation chamber at 37°C , 5% CO_2 , and 50–60% humidity using the Visual Basic for Applications macro 'AutofocusScreen'⁵⁷. Binarized images from Hoechst and PI channels were combined (H + PI) to calculate total cell area, while PI alone was used as a proxy for dead cells. Drug response curves to determine the LD50 were fitted if there was a significant difference between cell death in drug-treated and untreated samples (ANOVA with P -values < 0.0005), and area under curve (AUC) values were calculated for cell death. Cell growth was estimated by dividing total cell area (H + PI) at 72 h by total cell area (H + PI) at 0 h after drug application, and the area under curve for proliferation inhibition (AUC_{pi}) was determined. To correlate drug responses with scRNA-seq results, median cell cycle scores were calculated for each sample with the AddModuleScore function in Seurat, using previously published cell cycle genes⁵⁴.

Comparison of overall survival times. Overall survival (OS) was defined as the time from surgery to death or last follow-up. OS shorter than 90 days after surgery was considered peri-operative death and therefore excluded from the survival analyses. Median survival was estimated using the Kaplan–Meier method, patients still alive at the last follow-up were censored. Survival curves between groups were compared by the log-rank test. Analysis and plots were performed using the R packages survival and survminer.

Reporting summary. Further information on research design is available in the Nature Research Reporting Summary linked to this article.

Data availability

The single-cell sequencing data generated in this study have been deposited at the European Genome-Phenome Archive (EGA), which is hosted by the EBI and the CRG, under accession number EGAS00001004661. Primary PDAC scRNA-seq data was downloaded from the GSA (accession number CRA001160, samples T18 and T20). Gene ontology (GO) term analysis was performed using the MSigDB database v7.1 (<https://www.gsea-msigdb.org>). Gene interactions networks were identified using the STRING database v11 (<https://string-db.org>). Image data is available from the authors upon request. All other data are available within the Article or Supplementary Information.

Received: 3 September 2020; Accepted: 15 September 2021;

Published online: 05 October 2021

References

- Ryan, D. P., Hong, T. S. & Bardeesy, N. Pancreatic adenocarcinoma. *N. Engl. J. Med.* **371**, 1039–1049 (2014).
- Siegel, R. L., Miller, K. D. & Jemal, A. Cancer statistics, 2019. *CA Cancer J. Clin.* **69**, 7–34 (2019).
- Rahib, L. et al. Projecting cancer incidence and deaths to 2030: the unexpected burden of thyroid, liver, and pancreas cancers in the united states. *Cancer Res.* **74**, 2913–2921 (2014).
- Stark, A. P. et al. Long-term survival in patients with pancreatic ductal adenocarcinoma. *Surgery* **159**, 1520–1527 (2016).
- Strobel, O. et al. Actual five-year survival after upfront resection for pancreatic ductal adenocarcinoma: who beats the odds? *Ann. Surg.* <https://doi.org/10.1097/sla.0000000000004147> (2020).
- Jaffee, E. M., Hruban, R. H., Canto, M. & Kern, S. E. Focus on pancreas cancer. *Cancer Cell* **2**, 25–28 (2002).

7. Biankin, A. V. et al. Pancreatic cancer genomes reveal aberrations in axon guidance pathway genes. *Nature* **491**, 399–405 (2012).
8. Witkiewicz, A. K. et al. Whole-exome sequencing of pancreatic cancer defines genetic diversity and therapeutic targets. *Nat. Commun.* **6**, 1–11 (2015).
9. Waddell, N. et al. Whole genomes redefine the mutational landscape of pancreatic cancer. *Nature* **518**, 495–501 (2015).
10. Jones, S. et al. Core signaling pathways in human pancreatic cancers revealed by global genomic analyses. *Science* **321**, 1801–1806 (2008).
11. Bailey, P. et al. Genomic analyses identify molecular subtypes of pancreatic cancer. *Nature* **531**, 47–52 (2016).
12. Makohon-Moore, A. P. et al. Limited heterogeneity of known driver gene mutations among the metastases of individual patients with pancreatic cancer. *Nat. Genet.* **49**, 358–366 (2017).
13. Collisson, E. A. et al. Subtypes of pancreatic ductal adenocarcinoma and their differing responses to therapy. *Nat. Med.* **17**, 500–503 (2011).
14. Moffitt, R. A. et al. Virtual microdissection identifies distinct tumor- and stroma-specific subtypes of pancreatic ductal adenocarcinoma. *Nat. Genet.* **47**, 1168–1178 (2015).
15. Raphael, B. J. et al. Integrated genomic characterization of pancreatic ductal adenocarcinoma. *Cancer Cell* **32**, 185–203.e13 (2017).
16. Chan-Seng-Yue, M. et al. Transcription phenotypes of pancreatic cancer are driven by genomic events during tumor evolution. *Nat. Genet.* <https://doi.org/10.1038/s41588-019-0566-9> (2020).
17. Hayashi, A. et al. A unifying paradigm for transcriptional heterogeneity and squamous features in pancreatic ductal adenocarcinoma. *Nat. Cancer* **1**, 59–74 (2020).
18. Collisson, E. A., Bailey, P., Chang, D. K. & Biankin, A. V. Molecular subtypes of pancreatic cancer. *Nat. Rev. Gastroenterol. Hepatol.* **16**, 207–220 (2019).
19. Peng, J. et al. Single-cell RNA-seq highlights intra-tumoral heterogeneity and malignant progression in pancreatic ductal adenocarcinoma. *Cell Res.* <https://doi.org/10.1038/s41422-019-0195-y> (2019).
20. Bernard, V. et al. Single-cell transcriptomics of pancreatic cancer precursors demonstrates epithelial and microenvironmental heterogeneity as an early event in neoplastic progression. *Clin. Cancer Res.* **25**, 2194–2205 (2019).
21. Boj, S. F. et al. Organoid models of human and mouse ductal pancreatic cancer. *Cell* **160**, 324–338 (2015).
22. Seino, T. et al. Human pancreatic tumor organoids reveal loss of stem cell niche factor dependence during disease progression. *Cell Stem Cell* **22**, 454–467.e6 (2018).
23. Romero-Calvo, I. et al. Human organoids share structural and genetic features with primary pancreatic adenocarcinoma tumors. *Mol. Cancer Res.* **17**, 70–83 (2019).
24. Zhang, M. et al. Characterising cis-regulatory variation in the transcriptome of histologically normal and tumour-derived pancreatic tissues. *Gut* **67**, 521–533 (2018).
25. Lemstrová, R., Souček, P., Melichar, B. & Mohelnikova-Duchonova, B. Role of solute carrier transporters in pancreatic cancer: a review. *Pharmacogenomics* **15**, 1133–1145 (2014).
26. Kuhlmann, L. et al. Identification and validation of novel subtype-specific protein biomarkers in pancreatic ductal adenocarcinoma. *Pancreas* **46**, 311–322 (2017).
27. Chen, K. T. et al. Potential prognostic biomarkers of pancreatic cancer. *Pancreas* **43**, 22–27 (2014).
28. Rückert, F. et al. Co-expression of KLK6 and KLK10 as prognostic factors for survival in pancreatic ductal adenocarcinoma. *Br. J. Cancer* **99**, 1484–1492 (2008).
29. Muckenhuber, A. et al. Pancreatic ductal adenocarcinoma subtyping using the biomarkers hepatocyte nuclear factor-1A and cytokeratin-81 correlates with outcome and treatment response. *Clin. Cancer Res.* **24**, 351–359 (2018).
30. Roa-Peña, L. et al. Keratin 17 identifies the most lethal molecular subtype of pancreatic cancer. *Sci. Rep.* **9**, 11239 (2019).
31. Orsi, M. et al. Pancreatic cancer. *Imaging Tumor Response Ther.* **7**, 127–140 (2012).
32. Steele, C. W. et al. CXCR2 inhibition profoundly suppresses metastases and augments immunotherapy in pancreatic ductal adenocarcinoma. *Cancer Cell* **29**, 832–845 (2016).
33. Thomas, S. K., Lee, J. & Beatty, G. L. Paracrine and cell autonomous signalling in pancreatic cancer progression and metastasis. *EBioMedicine* **53**, 102662 (2020).
34. La Manno, G. et al. RNA velocity of single cells. *Nature* **560**, 494–498 (2018).
35. Javed, M. A. et al. Impact of intensified chemotherapy in metastatic pancreatic ductal adenocarcinoma (PDAC) in clinical routine in Europe. *Pancreatol.* **19**, 97–104 (2019).
36. Gillen, S. et al. Preoperative/neoadjuvant therapy in pancreatic cancer: a systematic review and meta-analysis of response and resection percentages. *PLoS Med.* **7**, 1–15 (2010).
37. Strobel, O., Neoptolemos, J., Jäger, D. & Büchler, M. W. Optimizing the outcomes of pancreatic cancer surgery. *Nat. Rev. Clin. Oncol.* **16**, 11–26 (2019).
38. Segovia, M. et al. Targeting TMEM176B enhances antitumor immunity and augments the efficacy of immune checkpoint blockers by unleashing inflammasome activation. *Cancer Cell* **35**, 767–781.e6 (2019).
39. Jabs, J. et al. Screening drug effects in patient-derived cancer cells links organoid responses to genome alterations. *Mol. Syst. Biol.* **13**, 955 (2017).
40. Ligorio, M. et al. Stromal microenvironment shapes the intratumoral architecture of pancreatic cancer. *Cell* **178**, 160–175.e27 (2019).
41. Juiz, N. et al. Basal-like and classical cells coexist in pancreatic cancer revealed by single-cell analysis on biopsy-derived pancreatic cancer organoids from the classical subtype. *FASEB J.* **34**, 12214–12228 (2020).
42. Raghavan, S., Winter, P. S., Navia, A. W., Williams, H. L. & DenAdel, A. The tumor microenvironment drives transcriptional phenotypes and their plasticity in metastatic pancreatic cancer. Preprint at <https://www.biorxiv.org/content/10.1101/2020.08.25.256214v2> (2021).
43. Tiriach, H. et al. Organoid profiling identifies common responders to chemotherapy in pancreatic cancer. *Cancer Discov.* **8**, 1112–1129 (2018).
44. He, Y. et al. Identification of key pathways and candidate genes in pancreatic ductal adenocarcinoma using bioinformatics analysis. *Oncol. Lett.* **17**, 3751–3764 (2019).
45. Puleo, F. et al. Tumor and microenvironment features. *Gastroenterology* **155**, 1999–2013.e3 (2018).
46. Budhwani, M., Mazzieri, R. & Dolcetti, R. Plasticity of type I interferon-mediated responses in cancer therapy: from anti-tumor immunity to resistance. *Front. Oncol.* **8**, 322 (2018).
47. Porter, R. L. et al. Epithelial to mesenchymal plasticity and differential response to therapies in pancreatic ductal adenocarcinoma. *Proc. Natl Acad. Sci. USA* **116**, 26835–26845 (2019).
48. Ootani, A. et al. Sustained in vitro intestinal epithelial culture within a Wnt-dependent stem cell niche. *Nat. Med.* **15**, 701–706 (2009).
49. Willert, K. et al. Wnt proteins are lipid-modified and can act as stem cell growth factors. *Nature* **423**, 448–452 (2003).
50. Stuart, T. et al. Comprehensive integration of single-cell data. *Cell* **177**, 1888–1902.e21 (2019).
51. McInnes, L., Healy, J. & Melville, J. UMAP: Uniform Manifold Approximation and Projection for Dimension Reduction. Preprint at <https://arxiv.org/abs/1802.03426> (2018).
52. Subramanian, A. et al. Gene set enrichment analysis: a knowledge-based approach for interpreting genome-wide expression profiles. *Proc. Natl Acad. Sci. USA* **102**, 15545–15550 (2005).
53. Liberzon, A. et al. Molecular signatures database (MSigDB) 3.0. *Bioinformatics* **27**, 1739–1740 (2011).
54. Tirosh, I. et al. Dissecting the multicellular exosystem of metastatic melanoma by single-cell RNA-seq. *Science* **352**, 189–196 (2016).
55. Szklarczyk, D. et al. STRING v11: protein–protein association networks with increased coverage, supporting functional discovery in genome-wide experimental datasets. *Nucleic Acids Res.* **47**, D607–D613 (2019).
56. Saelens, W., Cannoodt, R., Todorov, H. & Saeys, Y. A comparison of single-cell trajectory inference methods. *Nat. Biotechnol.* **37**, 547–554 (2019).
57. Conrad, C. et al. Micropilot: automation of fluorescence microscopy-based imaging for systems biology. *Nat. Methods* **8**, 246–249 (2011).

Acknowledgements

This work received financial support from NCT 3.0 Extension Programm (NCT3.0_2015.17 PrecO-Panc), DKFZ-HIPO (# HIPO-015 K20), PANC-STRAT—single cell sequencing extension (BMBF 01ZX1605C), the incubator grant sparse2big (# ZT-I-0007), European Commission (ESPACE, #874710 Horizon 2020), and the German Network for Bioinformatics Infrastructure (de.NBI) (# 031A537A, # 031A537C). S.L.B. and O.S. were supported by the National Center of Tumor Diseases (NCT) Heidelberg (NCT3.0_2015.17 PrecO-Panc). Human specimens and clinical data were obtained from the EPZ-Pancobank (Biobank of the European Pancreas Center at the Department of General Surgery, University Hospital Heidelberg) in accordance with the regulations of the tissue biobanks and an approval by the Ethics Committee of Heidelberg University (ethic votes 301/2001, 159/2002, S-206/2011, S-708/2019). Activities of the EPZ-Pancobank were supported by the Heidelberger Stiftung Chirurgie and in part by the German Ministry of Science and Education (BMBF) grants 01ZX1305C, 01ZX1605C, 01KT1506. The EPZ-Pancobank is chaired by Prof. Dr. M. W. Büchler, assisted by Dr. N. A. Giese, Dr. M. Schenk, and M. Fischer, and is a member of the BioMaterial Bank Heidelberg/BMBH (coordinator: Prof. P. Schirmacher, BMBF grant #01EY1701) belonging to the German Biobank Alliance. The authors thank K. Schneider, E. Lederer, and K. Ruf for the excellent technical support. The authors thank Martin Sprick for the helpful discussion.

Author contributions

O.S., C.C., and R.E. conceived the project, acquired funding, and provided supervision, with equal contributions. S.L. and J.J. planned and performed experiments with support from K.J. T.G.K. performed data analysis and wrote the paper. F.W.T., O.D., N.I., and

A.G. contributed to data analysis. C.S.L. contributed to survival data acquisition and analysis. All authors discussed the results and reviewed the final paper.

Funding

Open Access funding enabled and organized by Projekt DEAL.

Competing interests

The authors declare no competing interests.

Additional information

Supplementary information The online version contains supplementary material available at <https://doi.org/10.1038/s41467-021-26059-4>.

Correspondence and requests for materials should be addressed to Roland Eils, Oliver Strobel or Christian Conrad.

Peer review information *Nature Communications* thanks David Ting and the other, anonymous, reviewer(s) for their contribution to the peer review of this work. Peer reviewer reports are available

Reprints and permission information is available at <http://www.nature.com/reprints>

Publisher's note Springer Nature remains neutral with regard to jurisdictional claims in published maps and institutional affiliations.



Open Access This article is licensed under a Creative Commons Attribution 4.0 International License, which permits use, sharing, adaptation, distribution and reproduction in any medium or format, as long as you give appropriate credit to the original author(s) and the source, provide a link to the Creative Commons license, and indicate if changes were made. The images or other third party material in this article are included in the article's Creative Commons license, unless indicated otherwise in a credit line to the material. If material is not included in the article's Creative Commons license and your intended use is not permitted by statutory regulation or exceeds the permitted use, you will need to obtain permission directly from the copyright holder. To view a copy of this license, visit <http://creativecommons.org/licenses/by/4.0/>.

© The Author(s) 2021